An analysis of scatterometer returns from a water agitated by rain

Larry Bliven, Hubert Branger, Piotr Sobieski, Jean-Paul Giovanangeli

An analysis of scatterometer returns from a water surface agitated by artificial rain: evidence that ring-waves are the main feature

L. F. BLIVEN

NASA/Goddard Space Flight Center, Code 972 Wallops Island, VA 23337, U.S.A.

H. BRANGER

Institut de Mécanique Statistique de la Turbulence 12 av. du Général Leclerc, Marseille, France

P. SOBIESKI

U Catholique de Louvain, Département d'Electricité place du Levant 3, B-1348 Louvain-la-Neuve, Belgium

and J-P. GIOVANANGELI

Institut de Mécanique Statistique de la Turbulence 12 av. du Général Leclerc, Marseille, France

Abstract. Both wind and rain roughen the sea surface, but whereas wind generates waves, rain generates craters, stalks and ring-waves. Average backscattered power for scatterometer returns from water surfaces is closely related to small scale features on the water surface, so we use backscattered power from short wind-waves as a basis to evaluate the importance of ring-waves. Experiments were conducted with a 13·5 GHz scatterometer (30° incidence angle, vertical polarization) in a wind-wave tank that is enhanced by a rain simulator. Rain intensities ranged from 3-30 mm h^{-1} and wind friction velocities were between 10 and 50 cm s^{-1}. The variance of surface elevation for small scale features ξ^2_{sm}, i.e., ring-waves and short wind-waves, was computed for each case using data from a capacitance probe. Comparison of the data sets shows that the range of ξ^2_{sm} for the rain cases is comparable to that from light to moderate wind cases—so ring-wave amplitudes are not negligible. Analysis of the radar data provides evidence that ring-waves are the dominant feature contributing to the backscattered power. Thus ring-waves need to be included in scatterometer numerical models that contain rain effects.

1. Introduction

Improved rain and surface wind measurements in oceanic regions will make significant contributions to weather monitoring and climate studies. Spaceborne instruments such as altimeters and scatterometers measure power levels of microwave echoes from the sea-surface and since echo strength correlates with sea-surface roughness, particularly small-scale roughness, any processes that affects sea-surface roughness can modify measurements. Nearly ubiquitous winds roughen the sea-surface, so most data inversion algorithms deal with wind exclusively. Rain, however, also agitates the sea surface.

When a water drop hits a water surface, it can generate a cavity with a crown, which collapses to form a vertical stalk of water, which subsides to spawn rings of gravity-capillary waves that propagate outward (Worthington 1882, Le Méhauté *et al.* 1987 and Le Méhauté 1988). At grazing angles, Wetzel 1990 found from laboratory investigations that stalks are the dominant feature contributing to the backscattered power. At incidence angles used from space, a dearth of data hampers validation of numerical models. Atmospheric attenuation and scattering by rain are included in two models that simulate satellite based systems: at nadir by Meneghini and Atlas 1986 and at scatterometer angles by Sobieski *et al.* 1991. So important atmospheric effects have been modelled but the effects of rain on the air/sea interface are yet to be included for space applications.

Case studies show that rain effects data from altimeters, scatterometers and SARs (Guymer *et al.* 1981, Fu and Holt 1982, Hawkins and Black 1983, Black *et al.* 1985, Srokosz and Guymer 1988) and that atmospheric corrections do not necessarily remove all biases (Black *et al.* 1985). So air-sea interaction processes need to be investigated. Laboratory data sets (Moore *et al.* 1979 and Bliven *et al.* 1988) indicate that (*a*) K_u-and K_a-band scatterometer backscattered power can be enhanced by water drops striking the air/water interface, and (*b*) that water surfaces agitated solely by light rains can yield about the same backscattered power as water surfaces roughened solely by light winds. Moreover for combined light winds and light rains, Bliven and Giovanangeli (1992) established that backscattered power can be well modelled as the sum of rain and wind contributions. At higher winds and rain rates, various physical processes may be important. Attenuation of wind-waves by rain generated turbulence in the water has measured by Tsimplis (1992), who found evidence that estimates of eddy viscosity coefficients by Manton (1973) are too large by two orders of magnitude, so it is questionable that wave/turbulence interaction is the dominant mechanism for wind-wave attenuation by rain. On the other hand, a model by Le Méhauté and Khangaonkar (1990) indicates that raindrop impacts on the water surface can be inhomogeneous and consequently rain may contribute to long-wave growth. Gravity-wave interaction with capillary-waves has been modelled by Kharif *et al.* (1989), who report asymmetries as a function of the angle between the propagation directions of the two wave-trains. For application to *in situ* conditions, this model needs to be extended to include the effects of randomly distributed drop impacts. A general solution for all combinations of wind and rain will require a model with various regimes. Certainly surface agitation by rain needs to be included in empirical data inversion algorithms and numerical models—but data are certainly necessary to guide development and assessment of theoretical models.

Since the pioneering investigations by Wright (1966 and 1968) and Bass *et al.* (1968), estimates of radar backscattered power for viewing angle in the range of 30 to 60° from nadir have been typically computed by representing the sea surface as a two-scale rough surface. The strengths and limitations of this formulation for wind-wave studies were reviewed by Plant (1990), who discusses that composite models are used to represent wind roughened seas as patches of short waves (Bragg scattering model) that are locally tilted by large wave components. There is considerable evidence that scatterometer measurements are highly correlated to wind friction velocity (Jones and Schroeder 1977, Li *et al.* 1989, Giovanangeli *et al.* 1991 and Bliven *et al.* 1992). There also is considerable evidence that short gravity and capillary waves are the dominant spectral region that supports the bulk of the momentum fluxes from the wind to the water surface (see Plant (1982) for a review and Geernaert *et al.* (1986) for a recent assessment). Both aircraft data obtained by Ross and Jones (1978) and Seasat data analysed by Glazman (1988) show that the effect of long-waves on scatterometer average backscattered power is small. With a recognition of these factors, the entire wavenumber spectrum is not needed for first order modelling of average quantities. Indeed, Keller *et al.* (1992) employed laboratory results to assess assumptions concerning physical processes used in scatterometer wind-retrieval algorithms developed for field applications. Consequently data from long fetches in wide wind-wave tanks can assist in development of application algorithms.

The Bragg theory is also useful for modelling scattering from ring-waves. For example scattering from ring-waves generated by a single drop was investigated by Wetzel (1990), who concludes that due to its small amplitude 'a perturbation approximation may legitimately be applied at microwave frequencies', and who uses Wright's (1966) model to effectively replicate backscattered power time series from a ring-wave.

Although Bragg scattering of microwaves from short wind-waves is widely used as the dominant mechanism in scatterometer models, rain generates cavities, stalks, and ring-waves, so measurements are needed to evaluate the role of these features. The purpose of this paper is to present an analysis of data from a K_u-band scatterometer that was operated at 30° incidence angle. The experiments were conducted in a laboratory wind-wave tank that is enhanced with a rain simulator. Measurements from exclusively rain and exclusively wind conditions are used to evaluate the importance of ring-waves to backscattered power for a scatterometer configuration.

2. Instrumentation

We conducted these experiments in the large IMST wind-wave tank, which is 40 m by 3 m by 2·5 m and described in detail by Coantic and Favre (1974). The operational water depth is approximately 1 m. Displacement of the air/wave interface is measured with a capacitance probe that is able to measure water level with a precision of 0·02 mm (static mode) and 0·08 mm (dynamic mode) for wave frequencies up to 20Hz. Maximum wind velocity is about $14\,\mathrm{m\,s^{-1}}$ and the longitudinal and vertical air velocity fluctuations (u' and w') are computed from hot film anemometer data using a non-linear cooling law by Giovanangeli (1980). Friction velocity u^* is computed using the covariance method, i.e., $u_* = \langle -u'w' \rangle^{1/2}$, where $\langle\rangle$ means time averaged.

A 13·5 GHz (2 cm wavelength) radar system was used in this study and its design is similar to the 36 GHz system described by Bliven *et al.* (1988). We use a standard procedure to calibrate the radars, i.e., the backscattered power from a 15 cm diameter metal sphere at the operational range is adjusted to a reference value. For each experimental condition, we digitize the analog signal from the scatterometer and compute the average backscattered power. The average values are normalized with respect to the sphere value to obtain relative backscattered power σ. The scatterometer alignment in the wave tank was at 30° inclination from nadir and vertical polarization was used for both transmit and receive horns. With this set-up, the radar footprint on a calm water surface is approximately a circle with a 16 cm diameter.

In the nature, rain rate statistics vary with both averaging duration and measurement area, such that higher maximum values generally correspond to shorter duration and/or smaller area. The dominant drop-size, however, is typically in the range of 1 to 3 mm. For use in the wave-tank, we built a rain simulator that produces 2·8 mm diameter water drops from 72 20-gauge nozzles, which were arranged in an 8 by 9 grid with 5 cm spacing.

3. Results and discussion

3.1. *Physical conditions*

The set-up for the experiments was such that a comparison of scattering from ring-waves and wind-waves can be performed. Figure 1 illustrates the physical set-up in the IMST wave-tank. We use a right-handed coordinate system with the positive x-axis pointing in the direction of the wind, the y-axis in the plane of the mean water surface and the z-axis positive up. The *rain simulator* was located in the wave-tank at 35 m from the up-wind beach and 1 m above the water surface. So the 2·8 mm diameter drops impact the water surface at about $4{\cdot}4\,\mathrm{m\,s^{1}}$ ($\sim$60 per cent of their terminal velocity) and we observed craters, stalks and ring-waves that were generated by the drop impacts. If natural conditions are modelled using the drop-size distributions measured by Burrows and Attwood (1949) and the terminal velocities of water drops in still air obtained from Gunn and Kinzer (1949), then the kinetic energy of the artificial rain that we produced is about 50 per cent less than that from natural rain for comparable rainfall rates. In a comprehensive study of topographic features generated by falling water drops, Hallett and Christensen (1984) found that craters, stalks and ring-waves are produced by drop splashes from 2·8 mm drops with impact velocities greater $\sim 3{\cdot}0\,\mathrm{m\,s^{-1}}$. It is also interesting to note that the kinetic engery of a 2·8 mm diameter droplet at impact is abut equivalent to that of a

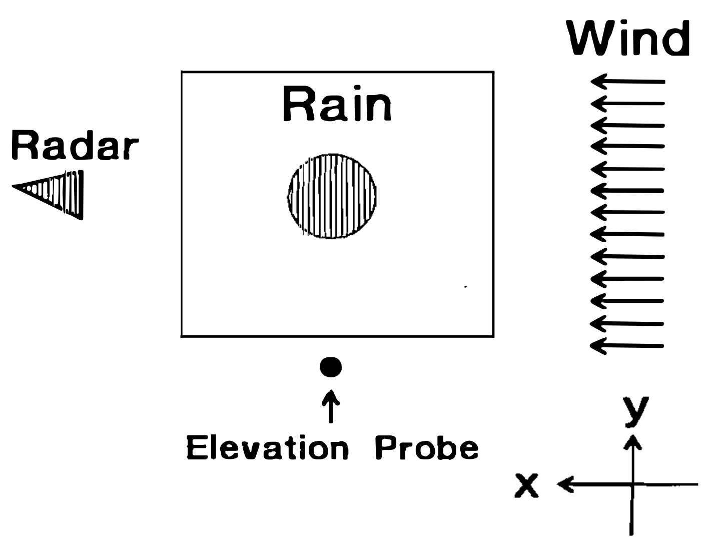

Figure 1. Physical set-up in the IMST wave-tank—top view.

2·1 mm diameter water drop at terminal velocity and that 2·1 mm diameter drops are close to the drop-size distribution maxima for rain rates in the range of 2·5 to 50 mm h^{-1}. The *capacitance probe* was located adjacent to the rain simulator (in the along wind direction, at the simulator centreline). Consequently it was just outside of the drop impact region and since craters and stalks do not propagate, the capacitance probe measured only ring-waves. The *radar* was located down-wind of the rain simulator and pointed up-wind at 30° from nadir, so that the microwave footprint was centred beneath the rain simulator and the radar measured backscattered power from all rain generated features (craters, stalks and ring-waves). θ is 0° for the scatterometer pointing upwind and this is denoted as σ^0. For wind cases, the capacitance probe measured waves and the scatterometer measured backscattered power from an up-wind viewing angle.

The *rain series* is summarized in table 1, which shows that the rain rates R ranged from 3–30 mm h^{-1}, so these observations simulate a large fraction of naturally occurring rains. Figure 2 shows that a linear model provides a high correlation for these K_u-band scatterometer observations. A linear model between σ and R was proposed by Bliven and Giovanangeli (1992), who simulated rain in the IMST wave tank and made measurements with a K_a-band scatterometer. The volume flow rate for the previous experiments was adjusted by changing the height between the nozzles and a reservoir. The rain simulator design has since been improved such that the volume flow rate is controlled by a regulated pump system and consequently the flow rates are set with an accuracy on the order of 1 per cent. These high quality K_u-band data together with the K_a-band data set provide evidence that a linear model between σ and rainfall rate is robust. Elevation variance ξ^2 provides a measure of the magnitude of surface features and thus is a basic factor affecting microwave scattering. The surface displacement ξ_{rms} of the ring-waves is certainly small since the 30 mm h^{-1} case produces an ξ_{rms} of only 0·07 cm. The dependence of ξ^2_{rms} on rain intensity from the simulator is displayed in figure 3, which shows that a linear model provides a reasonable fit to the data.

Wind series 1 is summarized in table 2, which shows that u_* ranged from 8 to 50 cm s^{-1}. A transition in wind boundary layer characteristics occurs at u_* $\sim$25 cm s^{-1} and it has been associated with the onset of air-flow separation and

Table 1. Rain series from IMST.

Rain rate (mm h^{-1})	ξ^2 (cm^2 10^{-4})	ξ^2_{sm} (cm^2 10^{-4})	σ^0
3·3	4·6	4·6	0·067
5·8	6·0	6·0	0·087
8·3	8·5	8·5	0·100
10·8	11·6	11·6	0·119
13·3	11·6	11·6	0·144
15·8	17·5	17·5	0·153
18·3	17·9	17·9	0·168
20·8	21·4	21·4	0·197
23·3	26·4	26·4	0·205
25·8	27·2	27·2	0·229
28·3	31·8	31·8	0·252
30·8	43·9	43·9	0·257

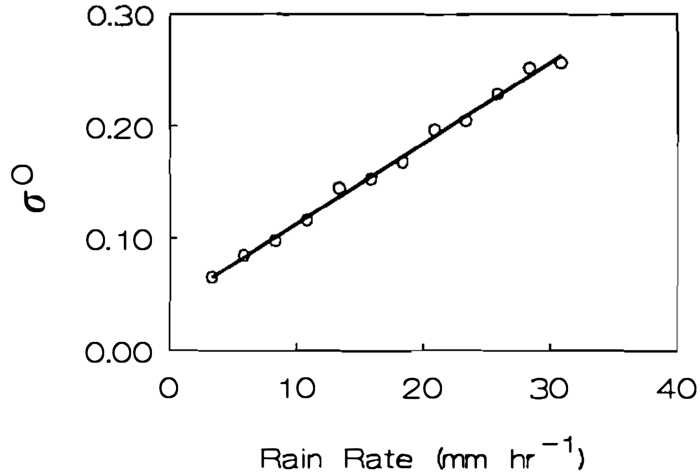

Figure 2. K_u-band scatterometer (30° incidence angle, vertical polarization) backscattered power as a function of rain rate in a wave-tank.

wave breaking (Wu 1969 a, 1969 b, 1980, 1986 and Melville 1977). Bliven *et al.* (1992) use this transition to develop a two segment scatterometer algorithm, which eliminates systematic errors that arise from using a single power law. So wind series I contains data from a broad range of conditions that correspond to both low and high wind regimes. The highest windspeed produced a ζ_{rms} of 1·8 cm, which is more than 25 times greater than the highest rain case. Comparison of the scatterometer data from the two series, however, shows that maximum σ's differ by only a factor of two (i.e., 3 dB). So it is evident that to obtain a robust relationship, an alternative parameter needs to be used to relate σ to the surface topography.

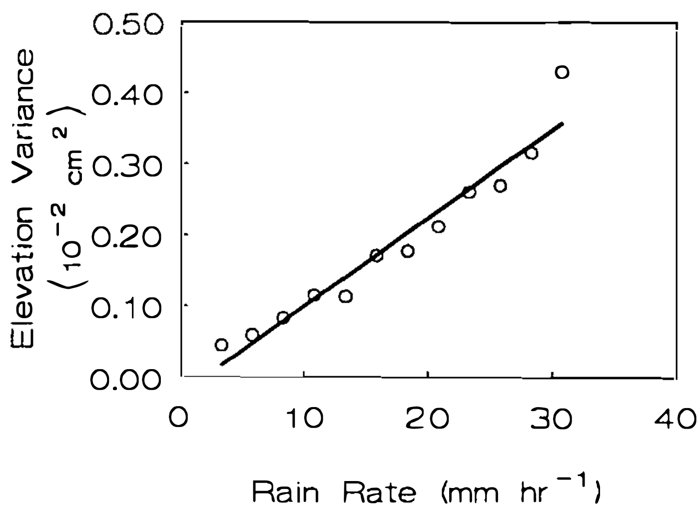

Figure 3. Surface elevation variance measured adjacent to the rain simulator as function of rainfall rate.

Table 2. Wind Series I om IMST.

u_* (cm s^{-1})	ξ^2 (cm^2 10^{-2})	ξ^2_{sm} (cm^2 10^{-4})	σ^0
8·0	4·0	2·7	0·049
10·1	9·7	3·2	0·038
11·3	12·2	4·1	0·044
14·9	25·7	5·7	0·057
17·4	49·4	13·4	0·092
22·7	70·5	23·7	0·174
26·9	107·3	35·1	0·244
32·7	180·8	52·0	0·296
38·3	246·8	74·7	0·377
47·0	336·4	107·0	0·473

The wavelength of first-order Bragg resonance between the transmitted 13·5 GHz microwaves and features on the water surface is 2 cm. Thus the surface-displacement power-spectral density of features with 2 cm projected wavelengths in the along-wind axis is a basic parameter for comparison of the rain and wind data sets. Waves with wavelengths of $2/\cos(\theta)$ cm, where θ is the angle between the radar viewing axis and the direction of propagation of the waves, satisfy the Bragg resonance condition for the data sets that we are examining. Surface-displacement wavenumber spectra are difficult to measure and instruments are not commercially available, so we take a pragmatic approach (that is common in wave studies) and use surface displacement measurements from a capacitance probe to deduce the dominant characteristics of the system. By using a linear dispersion relationship for capillary-waves, one finds that the resonance condition corresponds to a frequency of about 11·6 Hz for waves propagating along the radar viewing axis and a frequency of about 8·2 Hz for waves propagating along an axis 45° from the radar viewing axis. Frequency spectra of surface elevation were computed from the capacitance probe data to ascertain the characteristics of the rain cases and the characteristics of the wind cases.

Spectra for typical rain cases are presented in figure 4 and they are basically similar but the magnitude varies monotonically with rainfall rate. If the rain simulator generated a random distribution, then the frequency spectra would have no distinguishing features. A close examination of figure 4 reveals that there are a few peaks for each case and it is interesting to see that the peaks shift to higher frequencies as the rain intensity increases. This is because for each case the water droplets from the rain simulator produced nearly identical patterns on the water surface but the pattern timing varies as a function of rain intensity. For example, the drop rate of the nozzle closest to the capacitance gauge shows up as the lowest frequency peak, which is $\sim$1, 2, and 3 Hz for the 10·8, 20·8, and 30·8 mm h^{-1} rain rates. So these frequency spectra contain information related not only to surface wave characteristics but also to drop production periodicity—consequently the spectra can not be used to reliably estimate the magnitude of particular wavelengths. However, from visual observations of the water surface during the experiments it seemed that the wavelength of ring-waves was at most a few centimetres. In fact, video images made by Cavaleri (Wetzel 1990) of ring-waves from a 4 mm water drop show that the wavelengths are only a few centimetres and that the wave heights are

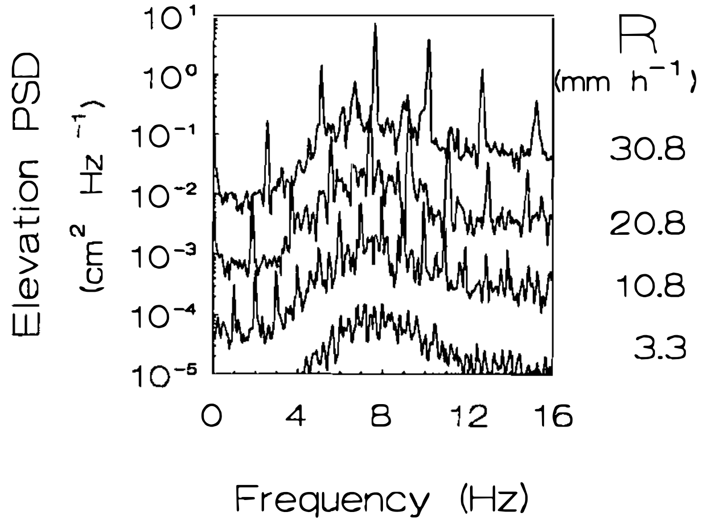

Figure 4. Frequency spectra of surface elevation for some rain cases. Successive cases are offset by powers of 10. Peaks shift to higher frequencies as the rain rate increases because the spectra contain information related not only to surface-wave characteristics but also to drop-production periodicity. The total elevation variance increases as rainfall rate increases and is attributable to gravity-capillary wavelengths.

on the order of a millimetre. Additionally, a model by Le Méhauté (1988) indicates that ring-waves concentrate in a band near the wavelength corresponding to the minimum group velocity (about 1·4 cm for clean water at room temperatures). So although the frequency spectra for the rain study cannot be converted to wave-number spectra, the total variance can be used as a representative measure of gravity-capillary wave amplitude.

Spectra for some wind cases are illustrated in figure 5, which reveals that a large fraction of wind-wave energy is attributable to frequency components that are less than 4 Hz (wavelengths > 10 cm). The high frequency tails from 8 to 16 Hz (wavelengths < 3 cm) are roughly parallel and their amplitudes are small. Since the surface displacement variance of the high frequency tails essentially corresponds to the spectral region of ring-waves, it is a sensible parameter to use in a first order analysis. These two quantities will be referred to as the small scale surface-elevation variance ξ^2_{sm}. The ξ^2_{sm} values from the rain series are within the range of $\xi^2{}_{sm}$ values from the wind series I.

3.2. *Ring-wave assessment*

3.2.1. *Scalar analysis*

Backscattered power measurements for the wind and rain studies are presented as a function of ξ^2_{sm} in figure 6. The rain and wind data sets follow slightly different trends so we first examine the wind data set by itself. A least squares model of the wind data shows that a linear relationship provides a reasonable fit between the backscattered power and the small scale variance, i.e.,

$$\sigma^0 = 0{\cdot}045 + 43{\cdot}36\ \xi^2_{sm}. \tag{1}$$

The backscattered power for the rain series is attributable to ring-waves plus other sources, which include craters and stalks. We simply use (1) to estimate the component of the backscattered power to assign to ring-waves. By this evaluation, on average nearly 70 per cent of the total backscattered power can be attributed to ring-waves and consequently ring-waves are a significant feature contributing to backscattered power.

3.2.2. *Directional factors*

Scatterometer measurements from wind generated waves are known to be dependent upon the radar azimuthal viewing angle. So the purpose of this section is to discern how directional factors affect the assessment of the importance of ring-waves.

The total nondirectional small-scale variance ξ_t^2 can be expressed as the sum of two components representing orthogonal axes in a Cartesian coordinate system. This is simply

$$\xi_t^2 = \xi_x^2 + \xi_y^2. \quad (2)$$

ξ_x^2 and ξ_y^2 are the magnitudes of the variance of the x- and y-components. Likewise, we define a total backscattered power as

$$\sigma_t = \sigma_x + \sigma_y. \quad (3)$$

$\sigma_x = (\sigma^0 + \sigma^{180})/2$ and $\sigma_y = (\sigma^{90} + \sigma^{270})/2$ are the average cross-sections for the radar aligned in the along- and cross-wind directions. A refinement to the assessment of the significance of ring waves is to compare relationships between σ_x and ξ_x^2 for both the wind and rain data sets.

We will use σ_x and ξ_x^2 to reconcile directional factors that affect the assessment of the importance of scattering from ring-waves. To estimate these variables, the

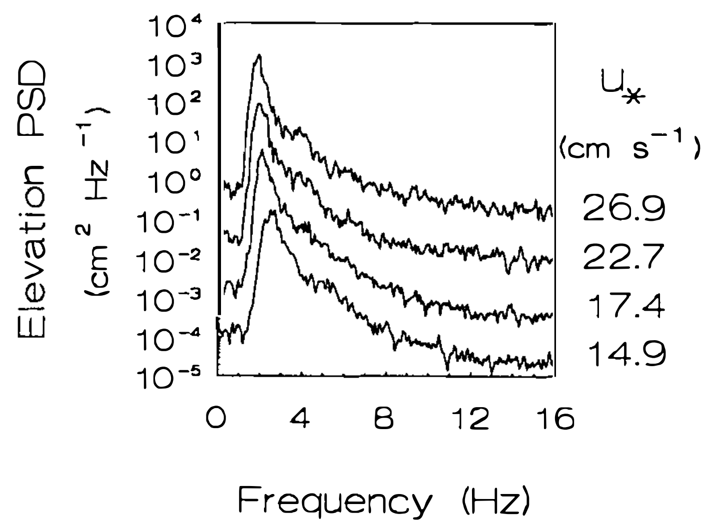

Figure 5. Frequency spectra of surface elevation for some wind cases. Successive cases are offset by powers of 10. A large fraction of the total elevation variance is from frequencies less than 4 Hz (wavelengths > 10 cm). The high frequency tails (> 8 Hz, i.e. wavelengths < 3 cm) are roughly parallel and their amplitudes are small.

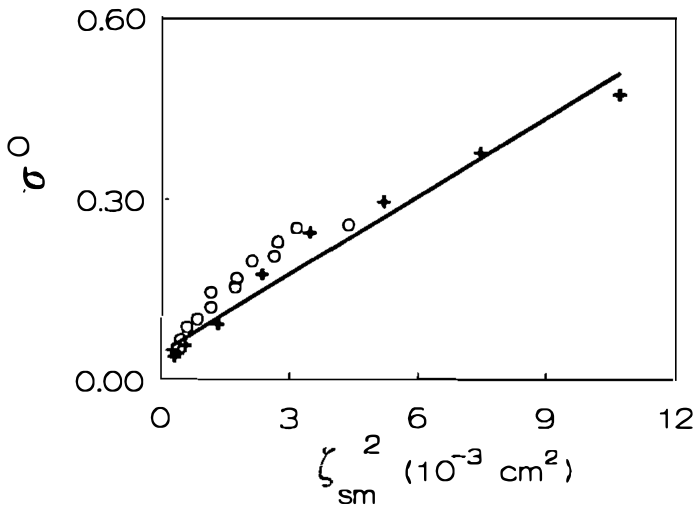

Figure 6. Up-wind scatterometer measurements *solely for rain* (O) and *solely for wind* (+) as a function of the total small-scale surface-elevation variance ξ^2. Application of the regression model from the wind conditions indicates that ring-waves are the dominant feature contributing to the backscattered power for rainy conditions.

scaling factor f_1 is used to obtain ξ_x^2 from ξ_t^2 and the scaling factor f_2 is used to obtain σ_x from σ^0. These scaling factors are

$$f_1 = \frac{\xi_x^2}{\xi_t^2}$$

$$f_2 = \frac{\sigma_x}{\sigma^0}. \tag{4}$$

For the rain cases the scaling factors are derived from a symmetry analysis as follows. Centred below the rain simulator is a region of capillary-gravity waves that is virtually isotropic, so $\xi_x^2 = \xi_y^2 = 0{\cdot}5\xi_t^2$. But because the wave gauge was positioned adjacent to the rain simulator, it measured ring-waves propagating only from angles ranging from approximately up-wind counter-clock-wise to down-wind, which is $\sim 180°$. Consequently $\xi_{sm}^2 = 0{\cdot}5\xi_t^2$ and thus $f_1 = 1$. Because ring-waves centred below the rain simulator are symmetric, azimuthal scans of scatterometer measurements from this region should also be cylindrically symmetric. Indeed an azimuthal scan with a K_a-band scatterometer (Giovanangeli *et al.* 1991) indicates that there is minimal directional asymmetry for cross-section measurements in the region centred below a similar rain simulator. Recall that the K_u-band scatterometer footprint is centred beneath the rain simulator, so $\sigma^0 \sim \sigma^{180}$ and consequently $f_2 = 1$.

For the wind cases, on the other hand, the scaling factors f_1 and f_2 cannot be characterized using just a symmetry analysis—we must use azimuthal measurements. In the wave-tank, wind-generated small-scale roughness completely surrounded the capacitance probe, so $\xi_t^2 = \xi_{sm}^2$. One parameter that is useful for characterizing the along-wind/cross-wind asymmetry is the magnitude of the ratio ξ_x^2/ξ_y^2, which can be estimated to first order by scatterometer measurements as follows. We suppose that small-scale wavenumber spectra in the along-wind and cross-wind directions have a similar shape, so application of the Bragg model (at a fixed incidence angle and polarization) yields

$$\frac{\sigma_x}{\sigma_y} \simeq \frac{\xi_x^2}{\xi_y^2} \tag{5}$$

This approximation is used to derive ξ_x^2 from ξ_t^2 for the wind cases. Azimuthal radar measurements were obtained when the K_u-band scatterometer of this study was operated at 95 m fetch in the large wave tank at Delft Hydraulics DH (Wanninkhof and Bliven 1991). At DH, the scatterometer was operated with vertical polarization and 30° incidence angle. An analysis by Giovanangeli *et al.* (1991), which characterizes radar measurements with respect to u_*, shows (*a*) that azimuthal characteristics of K_a-band scatterometer measurements (v-pol, 30° incidence) are similar for data obtained at the 35 m fetch in the wave-tank at IMST and at 95 m fetch in the wave-tank at DH, and (*b*) that the along-wind/cross-wind asymmetry of the scatterometer measurements are correlated to the along-wind/cross-wind asymmetry of small-scale features on the water surface. Wind series II is the K_u-band scatterometer data from DH, which are summarized in table 3 in terms of σ^0, σ^{180} and σ_y and u_* ranging from 7 to 100 cm s^{-1}. The data are typical in that $\sigma_x > \sigma_y$ and that σ_t *increases as* u_* increases. Figure 7 shows that the along-wind/cross-wind asymmetry of scatterometer cross-sections varies systematically as a function of u_*, so we computed f_1 for each wind case using the least-squares models given in figure 7. The scaling factor f_1 ranges from 0·67 to 0·82 for the IMST conditions, so the adjustments are small but not negligible. The second factor that needs to be considered is the upwind-downwind asymmetry in scatterometer backscattered power measurements. Again we use the Delft data set to estimate the scaling factor f_2 to obtain σ_x from σ^0. The data and model are plotted in figure 8, which show (*a*) that in the light wind regime, $\sigma^0 \sim \sigma^{180}$ and (*b*) that in the high wind regime, $\sigma^0 < \sigma^{180}$ such that the upwind-down wind scaling factor can be modelled as a linear function of u_*. We calculated f_2 values for the IMST conditions and the range of values is from about 1·03 to 1·10. Overall the scaling factors f_1 and f_2 produce adjustments that are small, which indicates (*a*) that the wind-waves tend to align in the direction of the wind, and (*b*) that the up-wind/down-wind asymmetry is almost negligible.

Table 3. Wind Series II from DH.

u^* (cm s^{-1})	σ^0	σ^{180}	σ_x	σ_y	σ_t
7·3	0·021	0·023	0·022	0·010	0·032
8·6	0·023	0·025	0·024	0·012	0·036
13·2	0·049	0·045	0·047	0·020	0·067
19·4	0·112	0·119	0·116	0·025	0·141
25·8	0·178	0·199	0·189	0·045	0·233
34·7	0·307	0·305	0·306	0·066	0·372
40·4	0·388	0·422	0·405	0·096	0·501
49·9	0·451	0·546	0·498	0·137	0·635
58·7	0·476	0·609	0·542	0·155	0·697
68·2	0·577	0·774	0·675	0·191	0·867
73·2	0·580	0·813	0·697	0·229	0·926
82·8	0·646	0·910	0·778	0·270	1·048
101·3	0·699	1·026	0·862	0·344	1·207

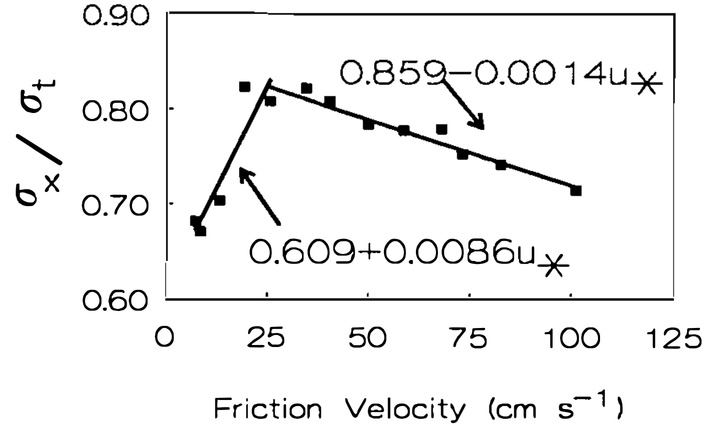

Figure 7. Scaling factor to derive the along wind component of ξ^2 for the wind cases.

Values of σ_x and ξ_x^2 were computed using the scaling factors for the rain and wind data sets. The results are shown in figure 9, which shows that the rain and wind data sets seem to commingle. We modelled the wind data set by itself and found that a least squares fit provides the following coefficients

$$\sigma_x = 0{\cdot}043 + 59{\cdot}11\xi_x^2. \tag{6}$$

To estimate the component of the total backscattered power for the rain cases that is attributable to scattering from ring-waves, we apply the directional wind model given by (6). The component of backscattered power associated with ring-waves is 90 per cent of the backscattered power from the rain-agitated water surface. The 10 per cent residual is ascribed to scattering from other features and/or unresolvable errors. So this analysis provides further evidence that scattering from ring-waves is the dominant mechanism and that backscattered power from other sources is small.

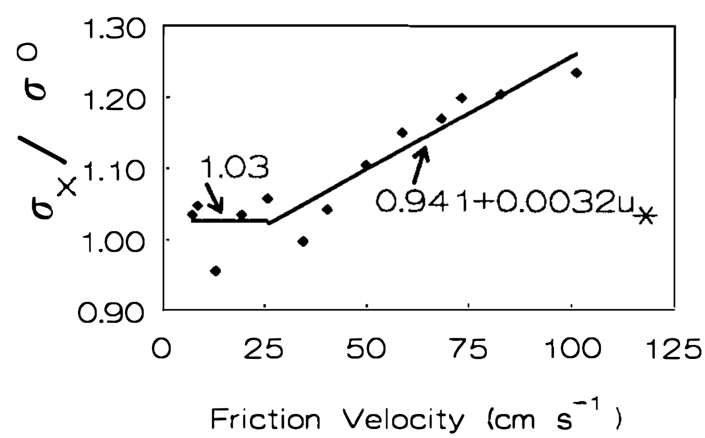

Figure 8. Scaling factor to derive σ_x for the wind cases.

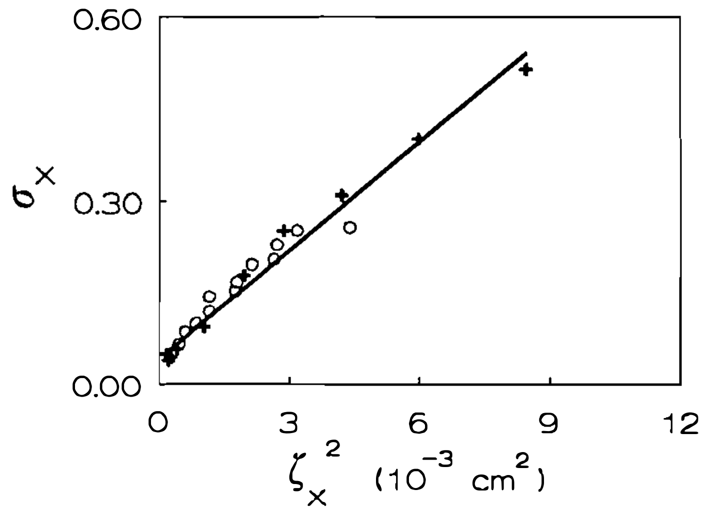

Figure 9. *Along-wind* scatterometer values solely for rain (O) and solely for wind (+) as a function of *the along wind component of* ζ^2. Application of the regression model from the wind conditions indicates that ring-waves are the primary feature contributing to the backscattered power for rainy conditions.

4. Summary and conclusions

In this paper we analysed scatterometer backscattered power and water-surface elevation data from rain and wind simulations in a large wave tank. The main results are (*a*) that the elevation variance of rain-generated ring-waves is the same order of magnitude as from short wind-waves, and (*b*) that ring-waves are the dominant feature contributing to backscattered power at scatterometric incidence angles from rain agitated water surfaces. From these findings, we conclude that scattering from ring-waves needs to be included in numerical models for geophysical interpretation of K_u-band scatterometer data.

Unquestionably this conclusion is derived from a limit data set (vv polarization at 30° from nadir) and further investigations are warranted to verify and refine this assessment. Likewise the conclusion by Wetzel (1990) that stalks are the dominant mechanism contributing to backscattered power has been corroborated by measurements only at 75° from nadir. Analysis of data from angles close to either extreme are likely to produce similar results—but at intermediate angles, the relative contribution from stalks, craters and ring-waves needs to be measured to validate scaling relationships.

Acknowledgments

Thanks to our colleagues at IMST who participated in this research and in particular to P. Chambaud for assistance with calibration of the hot film anemometer and the capacitance wave gauge. NASA (RTOP 972-461-131-08), Office of Naval Research (ONR 972-146-70-11), the Centre National de la Recherche Scientifique, the Direction des Recherches, Etudes et Techniques and the PAMOS Committee contributed funding for this research.

References

BASS, F. G., FUKS, I. M., KALMYKOV, A. I., OSTROVSKY, I. E., and ROSENBERG, A. D., 1968, Very high frequency radiowave scattering by a disturbed sea surface. *I.E.E.E. Transactions on Antennas and Propagation*, **AP-16**, 560–568.

BLACK, P. G., GENTRY, R. C., CARDONE, V. J., and HAWKINS, J. D., 1985, Seasat microwave wind and rain observations in severe tropical and midlatitude marine storms. *Advances in Geophysics*, **27**, 198–278.

BLIVEN, L., and GIOVANANGELI, J-P., 1993, An experimental study of microwave scattering from rain- and wind-roughened seas. *International Journal of Remote Sensing*, **14**, 855–870.

BLIVEN, L. F., GIOVANANGELI, J-P., and NORCROSS, G., 1988, A study of rain effects on radar scattering from water waves. *Proceedings of the 7th Conference on Ocean-Atmosphere Interactions of American Meteorological Society held in Anaheim, California*, on 1–5 February 1988 (Boston, MA: Am. Met. Society), pp. 230–233.

BLIVEN, L., GIOVANANGELI, J-P., WANNINKHOF, R. W., and CHAPRON, B., 1993, A laboratory study of friction velocity estimates from scatterometry: low and high regimes. *International Journal of Remote Sensing*, **14**, 1775–1786.

BURROWS, C. R., and ATWOOD, S. S., 1949, Drop-size distribution. In *Radar Handbook*, edited by M. I. Skolnik (New York: McGraw-Hill Book Company, 1970), p. 24.

COANTIC, M., and FAVRE, A., 1974, Activities in and preliminary results of air-sea interaction research at IMST. *Advances in Geophysics*, **16**, 391–405.

FU, L., and HOLT, B., 1982, Seasat views oceans and sea ice with synthetic-aperture radar. NASA-JPL publication 81-120.

GEERNAERT, G. L., KATSAROS, K. B., and RICHTER, K., 1986, Variations of the drag coefficient and its dependence on the sea state. *Journal of Geophysical Research*, **91(C6)**, 7667–7679.

GIOVANANGELI, J-P., 1980, A nondimensional heat transfer law for a slanted hot film in water flow. *DISA Information*, **25**, 6–9.

GIOVANANGELI, J., BLIVEN, L., and LE CALVE, O., 1991, A wind-wave tank study of the azimuth response of a K_a-band scatterometer. *I.E.E.E. Transactions on Geoscience and Remote Sensing*, **29**, 143–148.

GLAZMAN, R. E., PIHOS, G. B., and IP, J., 1988, Scatterometer wind-speed bias induced by the large-scale component of the wave field. *Journal of Geophysical Research*, **93**, 1317–1328.

GUNN, R., and KINZER, G. D., 1949, The terminal velocities of fall for water droplets in stagnant air. *Journal of Meteorology*, **6**, 243–248.

GUYMER, T. H., BUSINGER, J. A., JONES, W. L., and STEWART, R. H., 1981, Anomalous wind estimates from the Seasat scatterometer. *Nature*, **294**, 735–737.

HALLETT, J., and CHRISTENSEN, L., 1984, Splash and penetration of drops in water. *Journal de Recherches Atmosphériques*, **18**, 225–242.

HAWKINS, J. D., and BLACK, P. G., 1983, Seasat scatterometer detection of gale force winds near tropical cyclones. *Journal of Geophysical Research*, **88**, 1674–1682.

JONES, L. W., and SCHROEDER, L. C., 1977, Radar backscatter from the ocean dependence on surface friction velocity. *Boundary-Layer Meteorology* **13**, 133–149.

KELLER, R. M., KELLER, W. C., and PLANT, W. J., 1992, A wave tank study of the dependence of X-band cross sections on wind speed and water temperature. *Journal of Geophysical Research*, **97**, 5771–5792.

KHARIF C., GIOVANANGELI, J.-P., and BLIVEN, L., 1989, Rain waves-wind waves interaction and application to scatterometry. *IGARSS*, **3**, 1891–1896.

LE MÉHAUTÉ, B., 1988, Gravity-capillary rings generated by water drops. *Journal of Fluid Mechanics*, **197**, 415–427.

LE MÉHAUTÉ, B., and KHANGAONKAR, T., 1990, Dynamic interaction of intense rain with water waves. *Journal of Physical Oceanography*, **20**, 1805–1812.

LE MÉHAUTÉ, B., WANG, S., and LU, C. C., 1987, Spikes, domes, and cavities. *Journal International Association of Hydraulic Research*, **5**, 583–602.

LI, F., LARGE, W., SHAW, W., WALSH, E. J., and DAVIDSON, K., 1989, Ocean radar backscatter relationship with near-surface winds: a case study during FASINEX. *Journal of Physical Oceanography*, **19**, 342–353.

MANTON, M. J., 1973, On the attenuation of sea waves by rain. *Journal of Geophysical Fluid Dynamics*, **5**, 249–260.

MELVILLE, W. K., 1977, Wind stress and roughness length over breaking waves. *Journal of Physical Oceanography,* **7,** 702-710.

MENEGHINI, R., and ATLAS, D., 1986, Simultaneous ocean cross section and rainfall measurements from space with a nadir-looking radar. *Journal of Atmospheric and Oceanic Technology,* **3,** 400-413.

MOORE, R. K., YU, Y. S., FUNG, A. K., KANEKO, D., DOME, G. J. and WERP, R. E., 1979, Preliminary study of rain effects on radar scattering from water surfaces, *I.E.E.E. Journal of Oceanic Engineering,* **4,** 31-32.

PLANT, W. J., 1982, A relationship between wind stress and wave slope. *Journal of Geophysical Research,* **87,** 1961-1967.

PLANT, W. J., 1990, Bragg scattering of electromagnetic waves from the air/sea interface. In *Surface Waves and Fluxes,* edited by G. L. Geernaert and W. J. Plant (Amsterdam: Kluwer Academic Publishers), **2,** 41-108.

ROSS, D., and JONES, W. L., 1978, On the relationship of radar backscatter to wind speed and fetch. *Boundary Layer Meteorology,* **13,** 151-164.

SOBIESKI, P., GUISSARD, A., and BAUFAYS, C., 1991, Synergic inversion technique for active and passive microwave remote sensing of the ocean. *I.E.E.E. Transactions on Geoscience and Remote Sensing,* **29,** 391-406.

SROKOSZ, M. A., and GUYMER, T. H., 1988, A study of the effect of rain on Seasat radar altimeter data. *Proceedings of the IGARSS '88 Symposium held in Edinburgh, Scotland, on 13-16 September 1988,* ESA SP-284 (Paris: European Space Agency), pp. 651-654.

TSIMPLIS, M. N., 1992, The effect of rain in calming the sea. *Journal of Physical Oceanography,* **22,** 404-412.

WANNINKHOF, R. H., and BLIVEN, L. F., 1991, Relationship between gas exchange, wind speed, and radar backscatter in a large wind-wave tank. *Journal of Geophysical Research,* **96,** 2785-2796.

WETZEL, L. B., 1990, On the theory of electromagnetic scattering from a raindrop splash. *Radio Science,* **25,** 1183-1197.

WORTHINGTON, A. M., 1882, A study of splashes. *Proceedings of the Royal Society of London,* **34,** 217-229.

WRIGHT, J. W., 1966, Backscatter from capillary waves with application to sea clutter. *I.E.E.E. Transactions on Antennas and Propagation,* **AP-14,** 749-754.

WRIGHT, J. W., 1968, A new model for sea clutter. *I.E.E.E. Transactions on Antennas and Propagation,* **AP-16,** 217-223.

WU, J., 1969a, Wind stress and surface roughness at air-sea interface. *Journal of Geophysical Research,* **74,** 444-454.

WU, J., 1969b, A criterion for determining air-flow separation from wind waves. *Tellus,* **21,** 707-713.

WU, J., 1980, Wind stress coefficients over sea surface near neutral conditions—a revisit. *Journal of Physical Oceanography,* **10,** 727-740.

WU, J., 1986, Roughness elements of the sea surface—their spectral composition. *Telus,* **38A,** 178-188.